Phase Separation Mechanism in Gelling Aqueous Biopolymer Mixture Probed by Light Scattering

*D. Leisner, M.C. Blanco, M.A. López Quintela**

Dept. Química Física, Facultad de Química, Universidad de Santiago, Av. das Ciencias s/n, E-15782 Santiago de Compostela, Spain

SUMMARY: Using time-resolved static and dynamic light scattering (DLS) we have studied the kinetics of phase separation in an aqueous gelatin/maltodextrin mixture upon fast cooling. The time evolution of the droplet radius is modelled for the monodisperse case under reaction-limited and diffusion-limited conditions and compared with the observed evolution of the mode associated with the droplet diffusion. For quenches to above the gelatin ordering temperature, nucleation and rather reaction-limited than diffusion-limited growth and late-stage coalescence of droplets with diameters up to 90 μm were concluded. Quenches to well below the gelatin ordering temperature seem to induce diffusion-limited growth or (delayed) spinodal decomposition (SD) to a phase-separated microstructure with slow late-stage coarsening. In deep quenches, a second slow SD or diffusion-limited cluster aggregation (DLCA) process becomes apparent from the evolution of the static structure factor; the process seems to be related to the maltodextrin gelation in the composite.

1. Introduction

The stabilization of mixtures containing partly incompatible biopolymers is of interest in the development of formulations with controlled textural properties for dairy products. Just a relatively high kinetic stability of a microphase-separated mixture is required: an intermediate morphology, evolved by a slow phase separation process, must be stabilized by a gelation process that proceeds in parallel and is controlled by certain processing variables (e.g. temperature). A gelation process modifies the thermodynamic compatibility of the polymers in the evolving phases and thus the driving force for the phase separation. The process must be designed to finally trap the dispersed phase in the meshes of the gel at the desired scale of microphase separation. Pinning of the intermediate structure results from inhibition of hydrodynamic flows[1] which otherwise would drive its fast coarsening by coalescence[2].

In this work, we want to take a glance how physical gelation influences the kinetics of the phase separation process in an aqueous gelatin (LH1e)/maltodextrin (SA2) system. This process has already been investigated by time-resolved confocal laser scanning microscopy (CLSM) and turbidity measurements[3-7]. The thermodynamic incompatibility of the partly hydrolysed potato starch (maltodextrin SA2) and gelatin in the coiled conformation (above the triple helix melting temperature, ≅ 30 °C) has been investigated by quantitative analysis of coexisting phases[8] and mixing enthalpic measurements[9]. Based on CLSM, turbidity[6] and

 CCC 1022-1360/00/$ 17,50+.50/0

optical rotation results, an experimental binodal curve and its displacement upon gelatin triple helical ordering are available[3].

The gelation of the microphase-separated systems has been monitored by rheology[10,11]; on this basis, a gelation temperature diagram $T_g(c_1, c_2)$ is available[4]. Most of this work has been done applying an identical temperature vs. time profile for processing: individual polymer/water sample preparation at above 60 °C, careful (low-shear) mixing at 60 °C, linear cooling to the final temperature at -1 K/min only few minutes after mixing. However, measurements have also been performed in slower (-0.3 K/min) and faster (< -3 K/min) cooling conditions for comparison[4,5]. The results show that the standard cooling rate (-1 K/min) is mostly to be considered as a fast cooling if the final temperature is only slightly below the gelation temperature or higher if phase separation occurs by a slower nucleation and growth (NG) mechanism.

In the absence of gelatin, the kinetics of the maltodextrin gelation (which is accompanied by the formation of crystallites and thus turbidity increase) has been investigated by Kasapis[12]. For the concentration (c) and temperature (T) dependence of isothermal gel times (t_g), he found the relation

$$\lg(t_g / \mathrm{s}) = 0.038(T/°\mathrm{C}) - 4.53\lg(c/\%\mathrm{SA2}) + 8.67 \qquad (1)$$

The maltodextrin gelation in the absence of gelatin is thus very slow: even at 5 °C and concentration c = 12 %, it needs 3 h, and for c = 7 % already 24 h.

In the present work, we try to detect the phase separation mechanism as function of the depth of a fast quench into an immiscible region of the phase diagram, for a single near-critical composition. Cluster growth and phase separation will be detected by measuring the time evolution of the static and dynamic structure factors in light scattering, and by comparing with the turbidity evolution. Gel times will be estimated from time-resolved viscosity measurements. The observed changes in the scattering functions will be compared with the expected growth rates and time-dependent concentration distributions from two simple models for the growth of monodisperse spherical droplets in the reaction-controlled and diffusion-controlled limits. These models will therefore be presented in the following.

2. Growth simulation for monodisperse spherical droplets

Since the growth of nucleated colloidal particles in a matrix of the material (here biopolymer monomers) is a heterogeneous reaction, the most general mechanism involves diffusion of bulk material to the colloid surface, modification at its surface (active site) and finally aggregation to the colloid as a colloid constituent. Once aggregated to the colloid, the structure of the colloid may evolve by internal rearrangement in order to minimize the surface

energy. We will compare here only two extreme cases: diffusion-limited growth with fast internal colloid rearrangement as a consequence of an almost zero activation energy for the monomer uptake into the colloid or a considerably low bulk mobility, and reaction-limited growth with a considerably high activation energy for the modification/uptake reaction at the colloid surface, which allows the bulk concentration to equilibrate all the time. We do not consider cluster-cluster aggregation: clusters may grow only by monomer uptake. This corresponds to a Smoluchowski kernel[13] with $k(i,j) \propto i^{\mu}j^{\nu}$, $\mu << 0$ so that $k(i,1) >> k(i,j>1)$ where $k(i,j)$ is the bimolecular rate constant for aggregation of clusters consisting of i and j monomers.

2.1. Diffusion-limited growth in three dimensions with fast colloid rearrangement

Irreversible diffusion-limited colloid aggregation (DLCA) is a mechanism which leads to branched fractal colloids[14]; it includes formation of a system-spanning cluster above a critical concentration[15,16]. In the reversible case and if colloidal rearrangement is at least as fast as diffusion of bulk material to the liquid-like colloid surface, spherical droplets may evolve in order to minimize the surface energy. In a simplified model, we calculate the evolution of the droplet radius upon spontaneous nucleation of monodisperse spheres fixed on a ccp lattice, at time $t = 0$. The droplets grow only by diffusion of monodisperse monomers from an initially homogeneous liquid matrix to their surface. Although the late-stage behavior of a real process is dominated by cluster-cluster aggregation and the early-stage behavior is usually influenced by continuous nucleation and the resulting polydispersity, the early-stage characteristics of a triggered nucleation event that converts dilute inert, repulsive interacting macromolecules to sinks attractive for another major fraction of the macromolecules could be described satisfactorily by such a model.

Considering only the osmotic force, the integral monomer flux (dN_c/dt) to a droplet with radius R_c is proportional to its surface area $A = 4\pi R_c^2$ and to the concentration gradient at this surface, $(\partial c/\partial r)_{Rc}$. The diffusion equation for the monomers diffusing in three dimensions with a concentration-independent diffusion coefficient D along the radial coordinate r reads:

$$\frac{\partial c}{\partial t} = D\nabla^2 c = D\frac{\partial}{\partial r}\left(\frac{\partial}{\partial r} + \frac{2}{r}\right)c \qquad (2)$$

We consider a non-adiabatic boundary at $r = R_c$ and a semi-adiabatic boundary at $r = d_{cc}$. This second sink for the monomer concentration, taken also as radial symmetric, represents the first coordination sphere occupied with 12 neighbouring droplets. $n_c = 4\cdot(4\pi/3)/2^{3/2}$ droplets

have to be alimented exclusively from the sphere around a central droplet: the integral monomer flux to the shell at d_{cc} is n_c-1 or 4.924 times higher than that to the central sink at $r = R_c$. Starting values of droplet radius and homogeneous bulk monomer concentration are $R_c(t = 0) = R_{c0}$ and $c(r>R_c,t=0) = c_0$, corresponding to a final droplet volume fraction ϕ_∞ at the bulk monomer concentration c_{eq}. The sphere d_{cc} was divided into 10^4 shells of thickness dr. In one of about 10^5 equidistant time steps dt, the excess content of any shell, $(c-c_{eq})4\pi r^2 dr$, was allowed to walk the average walking distance $2(D dt/\pi)^{1/2}$ in positive and negative r directions weighted by the volumes of the final shells, and being reflected at the semi-adiabatic boundary. Since only walking distances of entire shell thickness dr appear as changes, the content is partitioned into neighbouring shells in that way that the average displacement is satisfied. If the jump ends at a shell with $r < R_c$, the corresponding amount of material enters the sink. R_c is updated after each time step and the (n_c-1)-fold quantity of what has entered to the central sink is withdrawn from the outer shells with $r > d_{cc}$-R_c. Figure 1 shows some results for the droplet radius evolution.

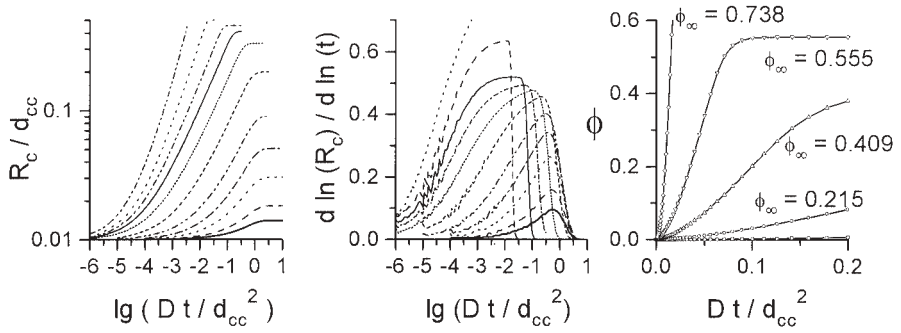

Fig. 1: Evolution of the droplet radius R_c and of the power of its change ($d\ln R_c/d\ln t$) with time, for initial droplet radius $R_{c0} = 0.01\ d_{cc}$. Maximum attainable ϕ from bottom to top: 1.65e-5, 3.55e-5, 1.67e-4, 7.79e-4, 4.45e-3, 0.0474, 0.215, 0.409, 0.555, 0.738, 0.888. The last graph shows some $\phi(t) \propto R_c^3(t)$ on linear scale.

We observe that the power exponent 0.5 is usually the upper limit for the growth of the radius with time for droplet volume fractions below the droplet-overlap threshold. For low final droplet volume fractions, the maximum slope could be as low as 0.1 or less, and the time range where it could be observed is much less than one decade. The early stage increase in the droplet volume $\phi \propto R_c^3$ is faster than linear, with the limit $\phi(t) \propto t^{3/2}$, but never exponential. An exponential increase in $\phi(t)$ might result if continuous nucleation would be considered.

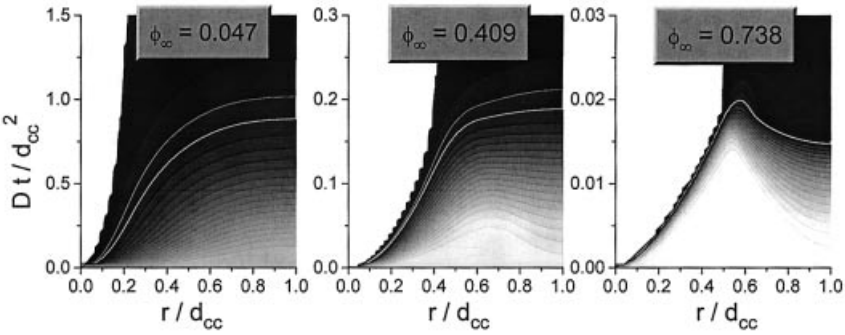

Fig. 2: Time dependence of the radial distribution of the bulk concentration of the monomer. From light grey to black: 1 to 0 times the initial excess concentration; white: central droplet.

Figure 2 shows three examples for the time dependence of the radial distribution of the bulk monomer concentration. The concentration at the colloid surface immediately drops to the equilibrium concentration c_{eq}, and a quasi-stationary monomer concentration gradient around the droplet establishes (depletion layer), which decreases proportionally to the average excess bulk concentration $\langle c(t) \rangle$ - c_{eq}. If the bulk concentration is not much lower than the concentration in the droplet (at high ϕ_∞), the rapidly expanding droplet always lets the gradient high; the depletion layer is a thin coating on the droplet. With decreasing ϕ_∞, the depletion layer becomes thicker and provides less contrast against the bulk. Generally, when ϕ has reached about 95 % of its final value ϕ_∞, depletion layers overlap and the growth slows down considerably.

The depletion layer provides a characteristic length in the radial distribution function and thus contributes a nonzero maximum to the static structure factor $S(q)$, at $q_m \geq 4\pi/d_{cc}$.

The time evolution of this maximum should be characterized by a continuous left-shift of q_m and an intermediate maximum of $S(q_m,t)$. q_m should be highest for high ϕ_∞, and the peak disappears when depletion layers overlap. This breakdown is almost sudden at high ϕ_∞ . In any case, there should be a second maximum of $S(q)$ due to the growth of the spheres, which is expected to evolve at lower q. We do not regard the periodic part from the ccp lattice model.

2.2. Reaction-limited growth in three dimensions

The growth of monodisperse spherical droplets with initial mass M_{c0} at time t=0 and mass density ρ, in a matrix with bulk monomer concentration c, is proportional to the actual excess bulk concentration c - c_{eq} and to the colloid surface, $(36\pi)^{1/3}(M_c/\rho)^{2/3}$:

$$\frac{\mathrm{d}(M_\mathrm{c}/M_\mathrm{cmax})}{\mathrm{d}t} = k'(1-M_\mathrm{c}/M_\mathrm{cmax})(M_\mathrm{c}/M_\mathrm{cmax})^{2/3} \tag{3}$$

with the rate constant

$$k' = k_1(c_0 - c_\mathrm{eq})\frac{(36\pi/\rho^2)^{1/3}}{1-M_\mathrm{c0}/M_\mathrm{cmax}} \tag{4}$$

$c_0 - c_\mathrm{eq}$ provides material to let the droplets grow to a maximum mass M_cmax; k_1 is the rate constant for the uptake of a bulk monomer to the droplet at its surface, and $k_{-1} = k_1 c_\mathrm{eq}$ is the rate for the dissociation of a monomer from the droplet which is also proportional to the surface, neglecting the effects of curvature since we are interested in the equilibrium for the final droplets with radii of several micrometers.

When at $M_\mathrm{c}/M_\mathrm{cmax} << 1$, the bulk concentration remains still close to its initial value, integration leads to an expression for the asymptotic behavior

$$\lim_{M_\mathrm{c}\to M_\mathrm{c0}} \frac{M_\mathrm{c}}{M_\mathrm{cmax}} = \left[\frac{k't}{3} + \left(\frac{M_\mathrm{c0}}{M_\mathrm{cmax}}\right)^{1/3}\right]^3 \tag{5}$$

Numerical integration yields the results presented in Fig. 3: the maximum exponent for the cluster mass increase with time is 3 and may be observed for even more than one decade of times, until the bulk concentration has decreased by about 10 %. The droplet radius $R_\mathrm{c} \propto M_\mathrm{c}^{1/3}$ increases about linearly with time in the range up to $R_\mathrm{cmax}/2$. The maximum growth rate for the mass is at $M_\mathrm{c}/M_\mathrm{cmax} = 0.4$ whereas for the radius it is at $t = 0$.

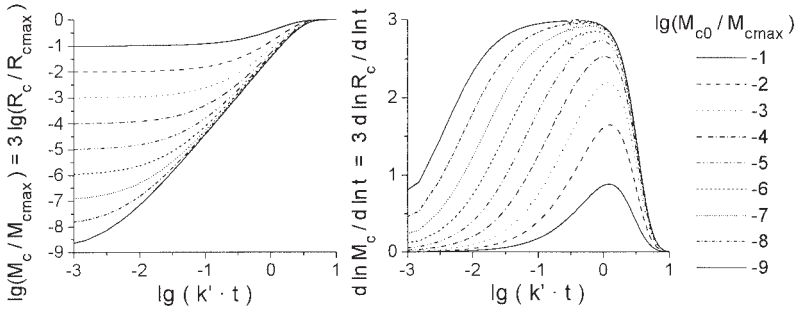

Figure 3: Evolution of the droplet mass M_c and of the power of its change ($\mathrm{d}\ln M_\mathrm{c}/\mathrm{d}\ln t$) with time for different initial droplet radii or masses M_c0.

3. Experimental

3.1. Sample preparation

Limed hide gelatin (LH1: Bloom 240, pI 4.7, M_n = 83300, M_w = 146 000) was provided from SKW Biosystems. Potato starch maltodextrin (Paselli SA2: glucose equivalent = 2, $M_n \cong$ 9000, highly polydisperse) was provided from Avebe. Samples (pH 6-7, ionic strength 0.01 M by NaCl) were prepared by mixing biopolymer and a filtered salt solution in bidistilled water, then gently stirring for 30 min at 60 °C (gelatin) or 95 °C (maltodextrin). The solutions were carefully mixed at 60 °C (about 1:1) and let in a stove for some 3 min with gentle shaking. Cylindrical cuvettes (1 cm external diameter, filled to 1/3, for light scattering) and standard quartz cuvettes (d = 2 mm, for UV/VIS spectroscopy) were stoppered tightly in order to avoid solvent evaporation.

3.2. Thermal ramping

"Rapid" exponential cooling from $T(t = 0)$ = 60 °C to temperatures T_∞, starting at time t = 0, was performed at cooling rates of dT/dt = -5 $min^{-1}\cdot(T-T_\infty)$ (light scattering) or -0.8 $min^{-1}\cdot(T-T_\infty)$ (UV/VIS); standard prethermostatted cell holders were used. 99 % (light scattering, viscosity) or 45 % (UV/VIS) of the initial temperature difference were equilibrated within 1 min. All final temperatures were maintained with at least 0.25 K absolute precision.

3.3. Dynamic light scattering

An ALV SP-86 goniometer equipped with a PMT detector and a Spectra Physics 127 helium-neon laser, operating at wavelength λ_o = 632.8 nm, was employed. Intensity data from θ = 90° angle reflections (at a scattering vector q = 18.7 μm^{-1}) were recorded and their time correlation analyzed by an ALV-5000 multiple-tau correlator (ALV, Langen, Germany). Normalized time-averaged intensity correlation functions $g_2^T(t)$ were accumulated initially for 30 s, the accumulation time increasing geometrically by a factor 1.05. All data were analyzed within the ergodicity approximation $g_2^T = g_2^E$, where g_2^E is the ensemble-averaged intensity autocorrelation function. The latter is linked to the electric field autocorrelation function g_1 by the Siegert relation: $g_1 = (g_2^E - 1)^{0.5}$. g_1, proportional to the dynamic structure factor, was thus fitted to a spectrum of exponential decays: $g_1 = \int A(\tau)\cdot\exp(-t/\tau)d\ln\tau$ by the CONTIN algorithm. We have obtained relaxation time spectra $A(\tau)$ in the τ range from 10^{-6} s up to 10^3 s on logarithmic scale. Assuming homodyne light beating and the absence of multiple scattering, the distribution of diffusivities D was obtained applying the relation $D = 1/(q^2\tau)$, where $q = (4\pi n/\lambda_o)\sin(\theta/2)$ is the scattering vector and n is the refractive index of the solution. The apparent correlation lengths $(\xi\cdot\eta/\eta_0)$ for cooperative displacements $\Delta r = q^{-1}$ of

inhomogeneities in the optical density were obtained applying the Stokes-Einstein relation, $D = kT/6\pi\eta\xi$, where the effective (dynamic-process-dependent) viscosity η takes values in the range from the solvent viscosity η_0 to the macroscopic viscosity.

3.4. Static light scattering

Ensemble-averaged intensity data from a slowly rotating sample were collected at 10 scattering angles θ; a single scanning cycle was completed within 84 s. Data from seven identical quenching experiments with coherent results were collected to enhance the time resolution.

3.5. Turbidity measurement

The simultaneous time (t) evolution of the transmittance of light at several wavelengths λ (532, 582, 632, 800 nm, away from absorption bands of the polymers) through a thermostatted quartz cuvette (path length d = 2 mm) was measured using an HP 8452A spectrophotometer equipped with deuterium lamp and diode-array detector, with the transmittance of the water-filled cuvette set to 1. The turbidity coefficient τ is calculated as $\tau(\lambda,t) = -\ln(\text{transmittance}(\lambda,t))/d$.

3.6. Viscosity measurement

Seven ml of a hot sample is poured into the cup of an SSA21 measurement system of a Brookfield DV2+ viscometer and the data acquisition is started ($t = 0$). The cup is lifted to its fixed position in the thermostatted jacket and the prethermostatted rotating spindle dives in. Temperature equilibration in the 1.2 mm thick gap is at least as fast as in the light scattering experiments. Continuous shear of less than 2 Hz (usually 0.28 Hz) is applied. The gel time t_g is approximated (though underestimated) by the time when a first linear increase in the measured torque starts to develop.

4. Results

We present time-resolved data for an off-critical composition in a ternary system of water and the biopolymers gelatin LH1 (4 %) and maltodextrin SA2 (7 %). The turbidity evolution will be analysed as a measure of generated interface by phase separation. The viscosity evolution was observed as a sensor for gelation. Dynamic light scattering results will be presented for the binary subsystems in order to identify the modes for the single polymers under identical conditions. Then the modes in the decomposed DLS spectra of the ternary system will be identified and analysed, taking into account the turbidity and viscosity information. Finally

static light scattering results are presented. The results are classified into two groups: (i) quenches above the gel melting temperature of gelatin which are generally quenches into a metastable region of the phase diagram, ii) quenches below this temperature where the evolution is influenced by gelation of the continuous gelatin-rich phase.

4.1. Turbidity evolution during phase separation

The optical density contrast on the length scale comparable to the wavelength of the incident light provides light scattering and thus turbidity. The relative refractive index difference of the phases is low enough to consider Rayleigh-Gans scattering, at least until SA2-rich droplets collapse and the carbohydrate starts to crystallize. The turbidity at a given wavelength then increases proportionally to the concentration of the interface and to the square of the refractive index difference between the separated domains. Figure 4 shows the evolution of the turbidity with time after fast quenches of the system to different final temperatures.

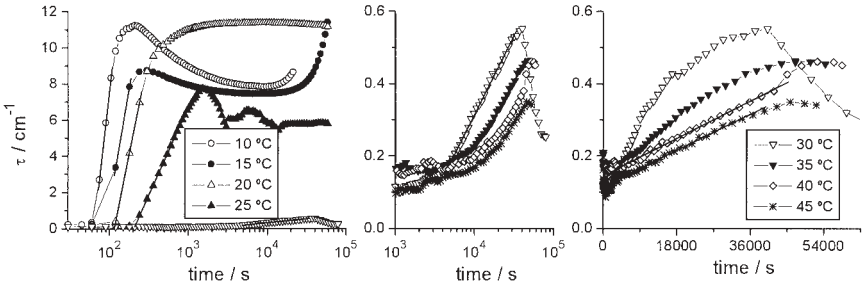

Fig. 4: Turbidity evolution at λ = 800 nm with time after a rapid quenching from 60 °C to different final temperatures.

Table 1: Delays for onsets of turbidity increase and rates of the turbidity increase.

T / °C	Onset t_1 / s	$(d\tau / dt)_{t>t1}$ / $cm^{-1}s^{-1}$	Onset t_2 / s	$(d\tau / d\ln t)_{t>t2}$ / cm^{-1}
45	2100 ± 500	$(5.6 \pm 0.1)\cdot10^{-6}$	--	--
40	1500 ± 500	$(5.8 \pm 0.1)\cdot10^{-6}$	(42000 ± 3000)	(0.17 ± 0.02)
35	1500 ± 1000	$(6.8 \pm 0.2)\cdot10^{-6}$	9400 ± 500	0.17 ± 0.02
30	700 ± 500	$(26 \pm 1)\cdot10^{-6}$	4400 ± 300	0.19 ± 0.01
25	--	--	220 ± 9	4.24 ± 0.03
20	--	--	117 ± 7	9.5 ± 0.2
15	--	--	96 ± 5	11.0 ± 2.0
10	--	--	66 ± 5	16.7 ± 0.4

After a delay of t_1 which is the longest for the shallowest quench (to 45 °C), the turbidity increases. The increase is linear in time for shallow quenches to final temperatures where

gelatin ordering does not yet occur (above 30 °C). In this regime, the rate of the linear turbidity increase, $d\tau/dt$, increases only slightly with the depth of the quench (see Table 1).

For a quench to 30 °C or below, another turbidity increase starts after a delay t_2. The rate of this turbidity increase *decreases* exponentially with time – the turbidity data (up to 70 % of the maximum) yield a straight line if displayed on logarithmic time scale. The data for 35 °C and 40 °C show both effects: first a linear turbidity increase with the rate similar to that at the higher temperature 45 °C and, after about 3 h (35 °C) or 12 h (40 °C), a faster but more time-dependent turbidity increase. The final turbidity value which corresponds to that of the upper phase in a bulk liquid-liquid phase separated system is identical for both temperatures but already higher than for the shallow quench to 45 °C.

For the quenches to 30 and 25 °C, a turbidity decrease is observed after a *late-stage* maximum was reached. The decrease was due to the beginning bulk phase separation. Whereas for the quench to 30 °C the final turbidity observed is very close to its equilibrium value in the upper phase, an equilibrium was not reached after the quench to 25 °C because, after about 1 h, the gelatin-enriched upper phase gels (see viscosity increase, Fig. 5), which precludes further sedimentation of droplets of the maltodextrin-enriched phase. Instead, the gelation boosts further incompatibility and a second wave of phase separation in the actual upper phase, as can be concluded from the observed new turbidity increase. This turbidity increase is not delayed because the concentration of small droplets (nuclei) is still high.

For the quenches to below 25 °C, the rapid viscosity increase (gelation) has the same delay as the first turbidity increase. This suggests that the large pregel clusters provide the necessary incompatibility for a subsequent fast phase separation parallel to the gelation process. The turbidity increases exponentially rather than linearly at an early-stage time and then turns to an intermediate-state maximum which is much higher than that observed at above 25 °C. For the quench to 20 °C, the turbidity maintains its high maximum value for a long time. Bulk phase separation is not observed after three days, not even for deeper quenches. Then, for quenches to 15 and 10 °C, turbidity decreases in a characteristic way, after the maximum of a similar height has been reached. This turbidity decrease will be discussed later (Section 5.2).

4.2. Viscosity evolution during phase separation and gelation

The gelation process is monitored by second-order changes in the viscosity evolution. The molecular weight of the gelling polymer is expected to critically increase to "infinite" in the vicinity of the sol-gel transition and formation of a percolation cluster. Thus an accelerated viscosity increase precedes gelation. A viscosity decrease would be expected to occur if the porosity of the interface between phases of different viscosity decreases. Upon bulk phase

separation, the measured system viscosity would approach the viscosity of the less viscous phase, which in a shear field could organize itself as a continuous film normal to the gradient of the shear if the shear force is stronger than the sedimentation force.

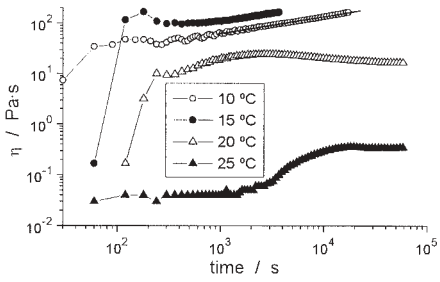

Figure 5: Time evolution of viscosity at a shear rate of 0.28 Hz or 2.8 Hz (▲) after rapid quench to various final temperatures

The viscosity increase due to gelation is observed after about 45 s (10 °C), 100 s (15 °C), 170 s (20 °C) or 4000 s (25 °C). For the lowest temperatures, the viscosity increases further with a power-law behaviour at a late stage. The fitted straight line in Fig. 5 yields the power exponent 0.332 ± 0.003. This might correspond to gelation of the dispersed phase. If the viscosity of the composite is proportional to the molecular weight of the filler, the dispersed carbohydrate clusters, at a constant monomer concentration (Staudinger relation), then the molecular weight of the clusters increases also with $t^{1/3}$, just as predicted for the Lifshitz-Slyozov diffusion-limited coarsening mechanism with a conserved order parameter[17]. In the case of the weaker gels formed at 20 and 25 °C, the system viscosity decreases slowly after a late-stage maximum was reached. The maximum itself is reached with a non-constant power of the curing time t. The power exponent is first larger than 1/3, much closer to 1 at T = 25 °C and, just before the maximum, it decreases to a value which is again close to 1/3. The exponent of 1 is indeed expected for a coarsening process driven by hydrodynamic flow[2,18], which at 25 °C is not immediately inhibited in the still large pores of the weak gel.

4.3. Dynamic changes upon cooling of *binary* aqueous biopolymer mixtures

Figure 6 shows dynamic light scattering data from quenching experiments with only one (though polydisperse) biopolymer present. Even at 60 °C, the temporary networks exhibit slow optical density fluctuations with relaxation times in the range from 5 to 50 ms, indicating inhomogeneities with Stokes radii of the order of 1 μm. In the maltodextrin samples, upon cooling, the Stokes radius shrinks to about half of its high-temperature value and then increases with time, whereas the scattering intensity already increases from the very beginning. One can almost certainly attribute the observed inhomogeneities (mode **d**) to large

branched amylopectin molecules. Upon a temperature decrease, the solvent becomes poorer in this carbohydrate, the branches collapse and let the molecule assume a more compact and dense structure ($\mathbf{d_1}$), which would also cause an increase in scattering intensity. The enhanced solvent-solvent interaction makes the molecules sensitive to hydrophobic intra- and intermolecular interactions and subsequent aggregation, as concluded from the further increasing scattering intensity and a slowing-down of mode $\mathbf{d_1}$.

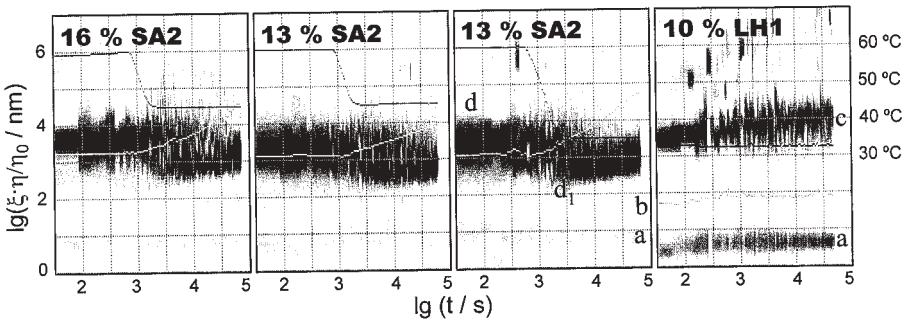

Figure 6: Time evolution of the dynamic structure factor for maltodextrin / water and gelatin / water binary mixtures upon slow (SA2) or fast (LH1) cooling from 60 °C. Grey scale: g_1 amplitude; dark grey line: temperature; light grey line: logarithmic static scattering intensity (two grids/decade).

In the gelatin solution, the slow mode (**c**) is due to the temporary gel which has to rearrange its crosslinks to fully relax fluctuation. The observed relaxation time of 30 - 100 ms in the 10 % LH1-containing aqueous solution then is the typical average lifetime of the temporary crosslinks[19]. This average increases with time since the most stable configurations (which might already include hydrogen bonds) survive longest. Below the helix-coil transition temperature (30 °C), helical ordering of the collagen-like molecules is favoured by synergistic hydrogen bonding in long-living triple-helical segments, and by percolation of molecules connected by these junctions physical gelation may occur.

The fast mode (**a**) indicates the correlation length ξ, the average mesh size of the temporal gel. Its increase with time in the case of the gelatin sample is in accord with the decrease in the concentration of total chain length in the system, due to partial triple-helical alignment. In the maltodextrin samples, the correlation length ξ diverges with time (modes **a**, **b**). Although this would have to be investigated in more detail, it could be related to partial gelation upon double-helical ordering of amylose and amylopectin fragments.

4.4. Quench of the LH1/SA2 mixture to above the gelatin ordering temperature

From CLSM with stained polymers, we know that upon shallow quenches (to between 50 and 30 °C), disperse maltodextrin-enriched spherical droplets from 2 to > 20 μm in diameter develop in the gelatin-enriched continuous phase and finally sediment as a bulk liquid phase. Our dynamic light scattering results for fast quenches to such temperatures are shown in Fig. 7. The gelatin modes are denoted **a** and **c**. The maltodextrin fast modes are **a** and **b**. The most intense mode, denoted **d**, belongs to the maltodextrin subsystem (amylopectin). As in the binary system, the major part ($\mathbf{d_1}$) of this mode becomes more rapid upon cooling (collapse of branches). The mode then by accident superimposes the less intense gelatin slow mode **c**. In contrast to the binary system, part of mode **d** maintains the high-temperature value and starts to slow down directly (mode $\mathbf{d_2}$). At 45 °C, this is the major part, whereas at 30 °C the minor one.

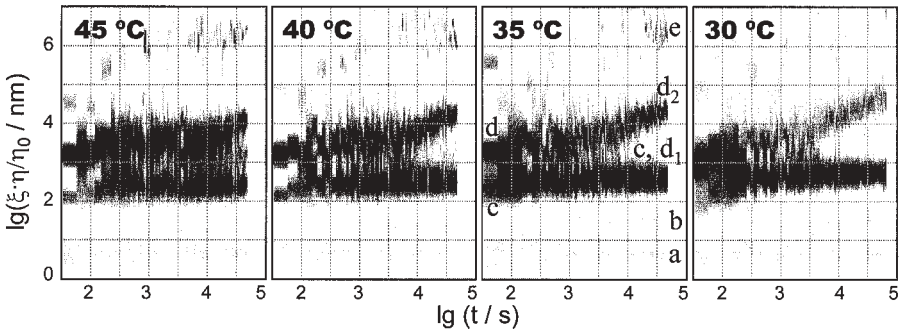

Fig. 7: Evolution of the relaxation spectrum with time after fast quench to various temperatures, at $q = 18.7\ \mu m^{-1}$. The grey scale is the almost linear g_1 amplitude, but the lowest amplitudes (> 0.002 A_{max}) appear enhanced for suitable contrast.

Obviously the presence of the gelatin inhibits the fast collapse of the amylopectin branches and makes them more susceptible to aggregation of faster diffusing linear amylose fragments, so that they grow to clusters and then droplets with Stokes radius $R_c = \xi(\mathbf{d_2})$. Since the size-dependent cluster viscosity is in between that of the solvent (water), η_0, and that of the macroscopic system viscosity, η, the figures indicate the upper size limit – the real radius could be about one order of magnitude smaller. The later observed mode **e** is due to sedimenting droplets formed by bulk liquid-liquid phase separation. We will focus our attention on the evolution of the cluster diffusion mode $\mathbf{d_2}$ presented in Fig. 8.

The apparent droplet radius is initially $\eta/\eta_0 \cdot (3.6 \pm 0.6)$ μm, increasing linearly with time. When it reaches about half of its observed maximum value, the growth rate decreases. This behaviour is similar to that predicted by the reaction-limited growth model (Section 2.2.). The

initial growth rate and the observed "final" radius (after 50 000 s) increase with decreasing temperature (see Table 2), whereas the intensity scattered from the droplets at q = 18.7 μm^{-1} remains almost unaffected – it even decreases with decreasing temperature and reaction time. Interestingly, the radial growth rate normalised to the droplet surface area remains virtually constant, indicating a curvature contribution to the kinetic rate constant.

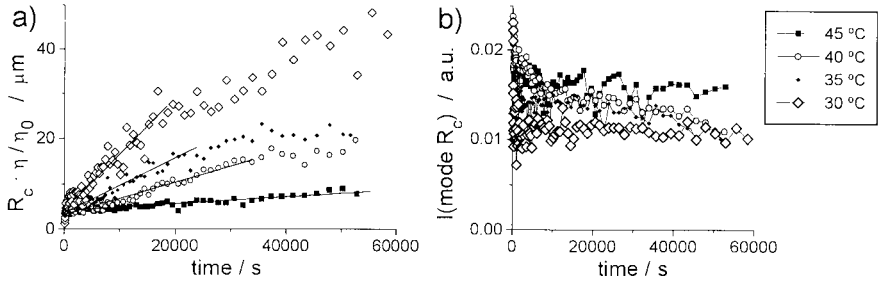

Fig. 8: Evolution of the droplet mode **d** – **d**$_2$ with time after quench. a) apparent Stokes radius, b) the mode amplitude in g_1 multiplied by the static scattering intensity.

Table 2: Initial and final (50 000 s) droplet radii, growth rate and intensity from Fig. 8.

T / °C	η/η_0	$R_{c0} \cdot \eta/\eta_0$ / μm	$R_{c\infty} \cdot \eta/\eta_0$ / μm	$dR_c/dt \cdot \eta/\eta_0$ / nm·s^{-1}	$dR_c/dt/(\eta/\eta_0)/R_{c\infty}^2$ / m^{-1}·s^{-1}	I_∞ / I_0
45	12 ± 2	4.1 ± 0.4	9 ± 1	0.08 ± 0.01	0.99 ± 0.34	0.90
40	12 ± 2	3.2 ± 0.4	19 ± 3	0.36 ± 0.03	0.98 ± 0.39	0.56
35	13 ± 2	3.6 ± 0.6	23 ± 3	0.60 ± 0.05	1.13 ± 0.39	0.66
30	14 ± 2	4.2 ± 0.9	45 ± 5	1.24 ± 0.10	0.61 ± 0.18	0.91

Since the droplets are at least four times larger than the inverse of the scattering vector, the mode scattering intensity should be proportional to the integral droplet surface (Porod's law). The decrease in the intensity shows that droplets either sediment or coagulate at lower temperatures. The enhanced tendency to coagulation can be explained by less repulsive droplet-droplet interaction potentials, which should decrease in the same manner as the activation energy for the monomer uptake by the droplet. In fact, the late-stage evolution of the droplet **d2** radius produces a slope close to 0.7 on the double-logarithmic plot of R_c vs. time (Fig. 7). A slope between 0.5 and 1 is expected for a coagulation mechanism in liquids[20], and a slope of 1/3 would be expected for the much slower Lifshitz-Slyozov ripening[17]. Since the system above 30 °C is still a rapidly fluctuating temporal network, hydrodynamic flows are not inhibited and activate coagulation and sedimentation. Mode **e**

appears together with macroscopic phase separation being indicative of macroscopic sedimenting droplets, since we observe the upper region of the sample.

4.5. Quench to below the gelatin helical ordering temperature

Figure 9 shows the same system quenched to below the helix-coil and gel-sol transition temperatures of gelatin. The gelation time coincides with the time when the fast slow-down of mode **c** ends; the mode then disappears because the infinite cluster becomes a homogeneous system and the pores become large-scale inhomogeneities. There is a crossover of modes **c** and **d** at the beginning of gelation. The stability of mode **d** indicates that amylopectin clustering is inhibited by the gelation of the metastable system. Large inhomogeneities, which could be attributed to dispersed clusters partially trapped in the polydisperse pore system, become apparent from mode $\mathbf{d_2}$ (phase microseparation).

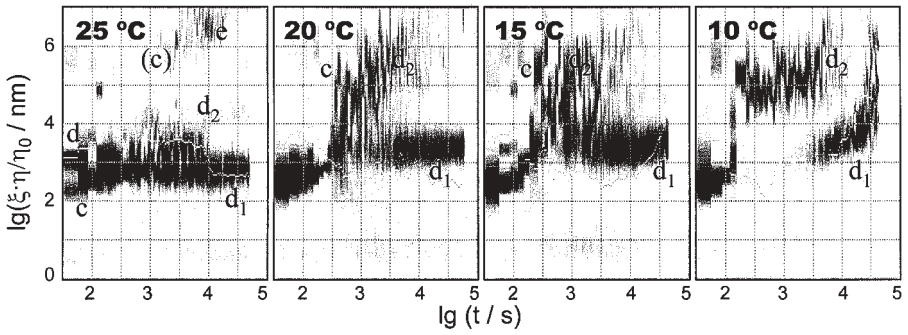

Fig. 9: Evolution of DLS spectra after temperature jump from 60 °C (cf. Fig. 5).

The evolution of the microdroplet radius R_c derived from the correlation length ξ of mode $\mathbf{d_1}$ ($R \cong \xi \cong$ 1-15 μm, using solvent viscosity) agrees with results from time-resolved confocal laser scanning microscopy (CLSM)[4]. This suggests that mode $\mathbf{d_1}$ corresponds to the fraction of dispersed clusters that can diffuse freely in gel pores on a length scale larger than $2\pi/q$; in this case larger than 336 nm. It is interesting to see that, even more extremely than at higher temperatures, in the late-stage evolution mode $\mathbf{d_1}$ is gaining intensity at the expense of mode $\mathbf{d_2}$. This indicates that smaller pores of the gelatin network, which trap the clusters of fraction $\mathbf{d_2}$, tend to disappear and the average pore size increases so that more and more carbohydrate clusters move "freely" on the observed length scale $2\pi/q$. The coarsening of the gelatin network microphase boundary is most likely due to a ripening mechanism with breaking and new formation of gelatin crosslinks.

Once the carbohydrate clusters are no longer isolated in separate pores of the early-stage gel, they become again subject to large-scale diffusion and cluster-cluster aggregation. Either

diffusion-limited cluster aggregation (DLCA) or spinodal decomposition (SD) becomes evident from the new exponential increase in both the relaxation time and the intensity of mode $\mathbf{d_1}$ in the late-stage evolution at 15 and 10 °C. At 10 °C, even the tendency to form an entire-pore-filling "infinite" cluster is evident from the divergent slowing-down of mode $\mathbf{d_1}$; this would correspond to the gelation of the dispersed phase.

A late-stage turn to a delayed isothermal SD process is unlikely except if the spinodal of the non-equilibrium system is moved by a slow process like polymerization, supramolecular complexation or physical gelation.

Time- and angle-resolved static light scattering results for quenches of increasing depth into the region below the gelatin ordering temperature are presented in Fig. 10. Although the data are very noisy and the resolution is poor, it can be seen that the static structure factor $S(q)$ increases first at higher q (corresponding to correlation distances $2\pi/q$ of about 400 nm).

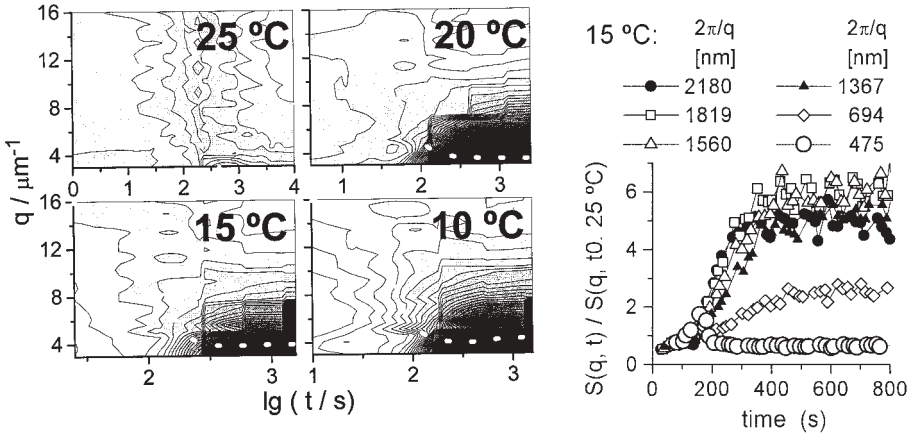

Fig. 10: Evolution of the static structure factor, $S(q,t) = I(q,T,t)/I(q,T_0=25\ °C, t_0=0)$, from 0.25 (white) to 6.25 (black), step size 0.25. The estimated $q_m(t)$ is indicated by a dotted line. Right-hand side: data obtained at 15 °C, on linear scale.

At $t \cong 150$ s, the intensity at $q > 10\ \mu m^{-1}$ passes through a sharp maximum and then decreases suddenly whereas, at the same time, the intensity at $q < 7\ \mu m^{-1}$ increases rapidly and from then on dominates the scattering function. Within the experimental uncertainty of the cooling rate, this is the time when the turbidity increases sharply. The position of the maximum of $S(q)$ at a given time t, $q_m(t)$, is roughly indicated by a white dashed line. It can be observed that q_m moves far out of the observed window at 25 °C, indicating a continued growth of the main correlation distance (e.g. of the droplet radius). Instead, at 20 °C and below, q_m apparently remains then close to 4 μm^{-1} and, at 10 °C, even turns to increase at later times.

There is a broad rather than a peaked maximum at the early stage, and possibly a second maximum at small angles just outside the experimental window.

The time evolution of the small correlation lengths was followed at enhanced time resolution. At fixed q = 18.7 μm^{-1} (see Fig. 11 and Table 3), rather an exponential than linear increase in the structure factor with time was observed – an exponential increase at q_m would be predicted for either the early stage of spinodal decomposition (SD) from the linear Cahn-Hilliard approach and, approximately, for DLCA. The PS mechanism will be discussed in Section 5.3.

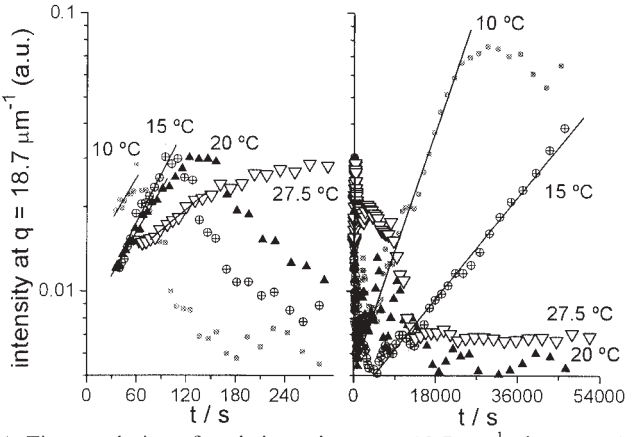

Fig. 11: Time evolution of static intensity at q = 18.7 μm^{-1} after quench.

Table 3: Fitting results from Fig. 11[a].

T / °C	1st SD or DLCA			2nd SD or DLCA		
	t_{start} / s	d ln$I$/dt /mHz	t_{max} / s	t_{start} / s	d ln$I$/dt /mHz	t_{max} / s
10	< 30	≥ 12	60	1500 ± 800	0.111 ± 0.003	30000
15	< 30	16 ± 2	100	4200 ± 500	0.047 ± 0.001	> 50000
20	≤ 30	12 ± 1	135	-- (> 50000)	--	--
27.5	70 ± 10	6 ± 1	280	-- (> 50000)	--	--

[a] t_{start} - beginning of the early-stage evolution during which the structure factor S increases exponentially; t_{max} - transition to late-stage behavior (maximum of scattering intensity I proportional to the product interface area x phase contrast product).

Both the first and the second exponential intensity increase become faster with decreasing temperature (increasing quench depth), ignoring the uncertain result for the first effect at 10 °C. The second process is about 300 times slower. The ratio of the rates can be taken as the

ratio of the effective diffusion coefficients in the two PS processes. This means that in the second process clusters rather than monomers must move and that the viscosity has increased considerably: the process starts after gelation of the continuous phase.

5. Discussion

The turbidity data show three different kinds of time evolution, indicating different phase separation (PS) processes to take place, sometimes even two at the same time. They will be examined by comparison of the simultaneous evolution of the scattering function $I(q)$ and its integral (turbidity), the decomposed dynamic structure factor, and the macroscopic viscosity.

5.1. Evolution after shallow quench

Above 27.5 °C, where no specific gelatin self-association to triple-helical segments was observed from optical rotation measurements[3], the turbidity increase starts linearly with time, indicating a linear increase in weight-average molecular weight M_w of the clusters and almost constant optical contrast. The evolution is quite similar to that observed by other authors for smaller concentrations of maltodextrin[3,6]. This PS process can be followed by the evolution of mode **d2** in the decomposed DLS spectra (Fig. 7). A late-stage power exponent ($d\ln(\xi\eta)/d\ln t = 0.7 \pm 0.07$) of this mode indicates that ripening of the corresponding droplet fraction by a combination of diffusion and hydrodynamically activated coagulation takes place, since the viscosity η is not expected to change so much. The droplet radii evolve from 1 to 45 μm (Table 2) before the mode becomes again faster and intensity decreases due to sedimentation of large droplets.

The delayed faster increase in the turbidity with the exponentially decaying rate under isothermal conditions has not been reported before (in this system). It is related to the evolution of mode **d1** (Fig. 7) and occurs also in the absence of gelatin (**d1** in Fig. 6). The turbidity growth law has the character of a slow relaxation process triggered by a critical thermodynamical shift at time t_2. This shift is apparently related to a slow sterically controlled collapse of some fraction of maltodextrin, starting at the temperature quench and proceeding at least until maltodextrin gelation. If a critical (concentration-dependent) degree of dehydration (deswelling) is reached at t_2, the intermolecular interaction becomes attractive and a NG process becomes nucleated: an Avrami-type kinetic model of the form $\tau = \tau_\infty \cdot \left[1 - \exp(-Z(t-t_2)^n)\right]$ (with Avrami exponent $n = 1$, indicative of a short grain-boundary-nucleation period just at t_2)[21] seems to fit the turbidity (τ) data well. Mode **d1** becomes the most intense one and slows down by no more than a factor of 1.5, corresponding

to a maximum cluster mass increase by a factor of 3.4 (at 30 °C), whereas the scattering intensity (turbidity) increases also by a factor between 2 and 3.6. This indicates that (if they are dense spherical droplets) the number of the small clusters remains constant after their nucleation at t_2, in accord with the Avrami exponent 1. The apparent critical radius of the nuclei (initial $\xi\eta/\eta_0$ of mode **d1**) is between 200 nm (at 45 °C) and 400 nm (at 30 °C). In CLSM experiments (with 500 nm resolution) under slow cooling conditions (-1 K/min), Lorén and Hermansson have seen "spherical droplets coming up all at the same time"[22], which confirms the triggered nucleation to take place. The carbohydrate fraction that forms the core of the nuclei is most likely the highly branched amylopectin: these molecules have a high molecular weight like gelatin, which suggests that they are more compatible with this biopolymer and phase-separate later than the short-chain linear amylose segments. The low-molecular-weight amylose segments in turn may rapidly form the liquid droplets of mode **d2**, and later also build up the periphery of **d1** clusters. Before amylopectin collapses, its diffusion is very slow because of the swelled branches (mode **d** in Figs 6, 7), and its bimolecular interaction is repulsive because of the excluded volume. And finally, because of the long branches, it is the best candidate for a collapse delayed by the temporal network of the other polymer even after its equilibrium excluded volume would turn towards zero. A delayed collapse can be concluded from the delayed switch of mode **d** to mode **d1**.

5.2. Evolution after a deeper quench affected by gelation

After quenches to below 30 °C, gelatin is poised to transform to a physical gel with triple-helical junction zones. In the course of that transformation, first some coils are rearranged to helices. Then larger and larger clusters of this polymer are formed which get more and more incompatible with the low- and average-molecular weight fraction of the carbohydrate. Finally the clusters connect to a permanent gel with inclusions of dispersed maltodextrin-enriched droplets. However, bulk PS occurs instead of the formation of a system spanning strong cluster if the concentration of helical gelatin is not large enough for rapid gelation; this is the case at 27.5 and 25 °C.

In the decomposed DLS spectra (Fig. 8), mode **d1** behaves similarly to the **d1** at higher temperatures. However, the viscosity increase in the continuous gelatin phase shifts this mode to longer relaxation times and apparent hydrodynamic radii $\xi\eta/\eta_0$, except in the early stage. If the critical size of the nuclei is not altered by temperature, this observation can serve to estimate the change in mobility of these clusters due to gelation. The effective relative viscosity η/η_0 would be about 2.5 at 25 °C or 8 at 20 °C and below, considering a critical hydrodynamic radius of 400 nm just as at 30 °C. Such a "low" viscosity value in a gel of

much higher system viscosity (see below) indicates that the environment of the cluster is large pores filled with a semidilute polymer solution.

The time evolution of the droplet mode **d2** is apparently different from the linear NG evolution at above 30 °C. Just together with the gelation (viscosity increase, slow-down and disappearance of mode **c**), this part of mode **d** slows down within a minute by more than two orders of magnitude. The time resolution of the data is insufficient to resolve the growth law. We must note that also the system viscosity increases by up to 3.5 orders of magnitude upon gelation. A comparison of onsets and maxima of turbidity, viscosity, and viscosity-corrected ξ(**d2**) is given in Table 4. The ξ(**d2**), however, is underestimated if $\eta < \eta_{max}$.

Table 4: Comparative evolution of turbidity, system viscosity, and apparent mode **d2** droplet radius ξ(**d2**) calculated for $\eta = \eta_{max}$ (estimates by visual analysis of presented figures).

T / °C	Turbidity			Viscosity				DLS
	t_{onset} / s	t_{max} / s	τ_{max} / cm^{-1}	t_{onset} / s	t_{max} / s	η_{max} / Pa·s	η_0 / mPa·s	ξ(d2) / nm
10	66	200	11.5	20	100	50	1.32	5.3
15	96	280	8.8	60	200	200	1.15	1.8
20	117	4000	11.5	110	300	10	1.01	20
25	220	1900	7.7	1500	2500	0.05	0.90	285

The estimated ξ(**d2**) indicate that the mode is due to clusters of the same size as those for mode **d1** (or even less) with the only difference that they are trapped in the gel instead of in large pores.

The turbidity evolution yields the Avrami-type NG behavior (with Avrami exponent 1), before a high and roughly temperature-independent maximum value is reached. The gelation (viscosity increase) and the NG process (turbidity increase) are apparently not highly coupled. The viscosity evolution might seem more rapid than the turbidity evolution at the lowest temperatures because the cooling rate is effectively higher in the viscometer than in the UV/VIS cuvette. But even at 20 and 25 °C, when 40 s is not much compared with the time scale of the PS and gelation processes, onsets and maxima of turbidity and viscosity increase occur at significantly different times. The gelation process is much more sensitive to temperature changes than the NG process in this temperature interval.

From the temperature dependence of the initial slope of the turbidity increase (see Fig. 4), it becomes apparent that there is a critical temperature between 25 and 20 °C where the dependence increases very fast with decreasing temperature. At this temperature one could expect that the long-range cluster interaction potential turns from repulsive to attractive. At 10 °C, the slope is very similar to that at 15 °C, indicating that the growth process has almost

turned to its diffusion-controlled limit. The significant intermediate-stage decrease in the turbidity at 10 and 15 °C, where no bulk phase separation (or droplet sedimentation) occurs, can be satisfactorily explained. Aymard and Williams[6] have suggested that this is a result of a droplet growth to radii of several micrometers, which were observed by CLSM. The form factors of these droplets would peak entirely at q below a critical q value corresponding to the acceptance angle of the spectrometer, so that their scattering contribution to the turbidity is no longer considered. They checked the phenomenon with latex spheres. We do not observe any intensity decrease in static light scattering. Hence, a phase-contrast-changing phenomenon can be excluded, as it also would change the static light scattering intensity. Thus the phenomenon can qualitatively be taken as indication of continued coarsening, generating droplets with diameters of several micrometers.

The late turbidity increase (after more than 10^4 s) seems to be due to spinodal decomposition of the gelling dispersed phase, resulting in the formation of carbohydrate crystallites. It was also observed during gelation of high-concentrated (≥ 10 % SA2) gelatin-free systems quenched to these temperatures, after comparable times.

5.3. Identification of PS mechanism upon deeper quench: DLCA vs. SD

Upon the quenches to below 25 °C, the static structure factor starts its evolution with a broad maximum at $q_m \cong 15\ \mu m^{-1}$ (Fig. 10). At a wave vector slightly higher ($18.7\ \mu m^{-1}$), an almost exponential (accelerated) increase in the scattering intensity is observed at the early stage. Although both features could be explained by a SD process at its early stage[1], the high value of q_m would be exceptional for phase separation in not very viscous liquids. In the SD process, at the intermediate stage, q_m would be expected to shift to lower values with $S(q_m)$ still increasing exponentially. $S(q)$ should obey a dynamic scaling rule: $S(x = q/q_m) = S(q_m)\cdot 4x^2/(3+x^6)$, for an off-critical quench in binary mixtures[23]. For $q > 2\ q_m$, an asymptotic behavior $S(q) \propto q^{-4}$ should be observed, the same as the Porod regime for objects with smooth surfaces. For a quench through the critical point, the corresponding asymptotic behavior would be $S(q) \propto q^{-6}$. We observe instead $S(q/q_m > 2)$ decaying fastest with $q^{-3.25}$ in the early intermediate and with $q^{-5.05}$ at later stages, with the asymptotic behavior not holding for more than half decade of q. This indicates that the early generated interface is not smooth but is probably the interface of fractal clusters of aggregated colloids, and the later-stage, slowly changing $S(q)$ is influenced by minima from a hard-sphere-type form factor.

A more plausible interpretation of the data is thus in terms of a DLCA process. The broad peak at about $15\ \mu m^{-1}$ then corresponds to the mixed peak of fast-growing (diffusion-limited) small clusters (presumably around collapsing amylopectin) and of depletion layers around

them (depleted in carbohydrate), of comparable thickness as the initial cluster radius. At some critical cluster size and when depletion layers overlap and thus disappear, long-range cluster-cluster interaction potentials become attractive and unscreened, and clusters aggregate to large clusters by DLCA. This is the moment when the peak, due to the depletion layers, breaks down and q_m shifts to low values, even to q's outside the observed window, and an accelerated intensity increase is observed at q near the new q_m, changing later to something like a $t^{1/2}$ behavior Note the similarity of the observed intensity evolution at $2\pi/q > 1$ μm (Fig. 10b) and the DLCA-like modeled time evolution of $\phi(t)$ or the cluster volume (Fig. 1c) for $\phi_\infty \cong 0.5$. Final cluster radii of up to 4 μm were observed by CLSM for systems with 6 instead of 7 % of SA2 under otherwise identical conditions[4]. The radii would correspond to a final q_m of 1.5 μm^{-1}; SALS measurements would be helpful to confirm details of the PS process. So far, the late-stage coarsening has been indicated only by a characteristic slow turbidity decrease.

Acknowledgement

This study has been carried out with financial support from the Commission of the European Communities, Agriculture and Fisheries (FAIR) specific RTD programme, CT 96 1015, "Mixed Biopolymers - Mechanism and Application of Phase Separation". The study does not necessarily reflect Commission views and in no way anticipates its future policy in the area.

References

1. R. H. Tromp, A. R. Rennie, R. A. L. Jones, *Macromolecules* **28**, 4129 (1995)
2. E. D. Siggia, *Phys. Rev. A* **20**, 595 (1979)
3. N. Lorén, A-M. Hermansson, M. A. K. Williams, L. Lundin, T. J. Foster, C. D. Hubbard, A. H. Clark, I.T. Norton, E. T. Bergström, D. M. Goodall, *Macromolecules* **34**, 289 (2001)
4. N. Lorén, A.-M. Hermansson, *Int. J. Biol. Macromol.* **27**, 249 (2000)
5. N. Lorén, M. Langton, A.-M. Hermansson, *Food Hydrocolloids* **13**, 185 (1999)
6. P. Aymard, M.A.K. Williams, A. H. Clark, I. T. Norton, *Langmuir* **16**, 7383 (2000)
7. M. A. K. Williams, D. Fabri, C. D. Hubbard, L. Lundin, T. J. Foster, A. H. Clark, I. T. Norton, N. Lorén, A.-M. Hermansson, *Langmuir* **17**, 3412 (2001)
8. S. Kasapis, E. R. Morris, I. T. Norton, M. J. Gidley, *Carbohydr. Polym.* **21**, 249 (1993)
9. A. Cesàro, F. Cuppo, D. Fabri, F. Sussich, *Thermochim. Acta* **328**, 143 (1999)
10. S. Kasapis, E. R. Morris, I. T. Norton, R. T. Brown, *Carbohydr. Polym.* **21**, 261 (1993)
11. V. Normand, P.D.A. Pudney, P.Aymard, I.T. Norton, *J. Appl. Polym. Sci.* **77**, 1465 (2000)
12. S. Kasapis, E. R. Morris, I. T. Norton, A. H. Clark, *Carbohydr. Polym.* **21**, 243 (1993)
13. M. Tirado-Miranda, A. Schmitt, J. Callejas-Fernández, A. Fernández-Barbero, *Langmuir* **15**, 3437 (1999)
14. J. L. Burns, Y. Yan, G. J. Jameson, S. Biggs, *Langmuir* **13**, 6413 (1997)
15. J.-M. Jin, K. Parbhakar, L. H. Dao, K. H. Lee, *Phys. Rev. E* **54**, 997 (1996)
16. R. Jullien, A. Hasmy, *Phys. Rev. Lett.* **74**, 4003 (1995)
17. R. H. Tromp, R. A. L. Jones, *Macromolecules* **29**, 8109 (1996)
18. A. J. Bray, *Phys. Rev. E* **47**, 3191 (1993)
19. I. Dierking, *J. Phys. Chem. B* **104**, 10642 (2000)
20. M. C. Blanco, D. Leisner, C Vázquez, M. A. López-Quintela, *Langmuir* **16**, 8585 (2000)

21. G. J. Hopkin, H. K. D. H. Bhadeshia, in: *Proc. 21st Risø Int. Symp. Mater. Sci.: Recrystallization – Fundamental Aspects and Relations to Deformed Microstructure*, N. Hansen, X. Huang, D. Juul Jensen, E. M. Lauridsen, T. Leffers, W. Pantleon, T. J. Sabin, J. A. Wert (Eds.), Risø National Laboratory, Roskilde (Denmark) 2000
22. A.-M. Hermansson, private communication
23. H. Furukawa, *Physica A* **123**, 497 (1984)